PHOTONICS Research

Tuning exciton dynamics by the dielectric confinement effect in quasi-two-dimensional perovskites

Minghuan Cui,[1,†] Chaochao Qin,[1,4,†] Yuanzhi Jiang,[2] Shichen Zhang,[1] Changjiu Sun,[2] Mingjian Yuan,[2] Yonggang Yang,[1,5] and Yufang Liu[1,3,*]

[1]Henan Key Laboratory of Infrared Materials & Spectrum Measures and Applications, Henan Normal University, Xinxiang 453007, China
[2]Key Laboratory of Advanced Energy Materials Chemistry (Ministry of Education), College of Chemistry, Nankai University, Tianjin 300071, China
[3]Institute of Physics, Henan Academy of Sciences, Zhengzhou 450046, China
[4]e-mail: qinchaochao@htu.edu.cn
[5]e-mail: yangyonggang@htu.edu.cn
[†]These authors contributed equally to this work.
*Corresponding author: yf-liu@htu.edu.cn

Received 10 July 2023; revised 19 November 2023; accepted 8 January 2024; posted 9 January 2024 (Doc. ID 500205); published 1 March 2024

The dielectric confinement effect plays an essential role in optoelectronic devices. Existing studies on the relationship between the dielectric confinement and the photoelectric properties are inadequate. Herein, three organic spacers with different dielectric constants are employed to tune the exciton dynamics of quasi-two-dimensional (quasi-2D) Ruddlesden–Popper perovskite films. Femtosecond transient absorption spectroscopy reveals that the small dielectric constant ligand enables a weak dynamic disorder and a large modulation depth of the coherent phonons, resulting in a more complete energy transfer and the inhibition of a trap-mediated nonradiative recombination. Additionally, the increase in the bulk-ligand dielectric constant reduces the corresponding exciton binding energy and then suppresses the Auger recombination, which is beneficial for high-luminance light-emitting diodes. This work emphasizes the importance of dielectric confinement for regulating the exciton dynamics of layered perovskites.

https://doi.org/10.1364/PRJ.500205

1. INTRODUCTION

Three-dimensional (3D) organic–inorganic hybrid perovskite has become a promising photoelectric conversion material that is widely used in solar cells [1,2], light-emitting diodes [3–8], and semiconductor lasers [9,10]. Although 3D perovskite materials have achieved outstanding photoelectric conversion efficiency, the instability under atmospheric moisture hinders their large-scale commercial application [11–14]. To date, reduced-dimensional (two-dimensional, 2D) perovskites are considered to be the most successful attempt to solve the stability problem [11–13,15–19]. By involving hydrophobic organic cations, 2D perovskite destroys the crystal symmetry of 3D perovskite and breaks the limitation of the tolerance factor [20]. More importantly, its dielectric confinement and quantum confinement effects can lead to a large exciton binding energy and special photophysical characteristics [21–24].

It is known that the dielectric confinement effect exists in quantum well structures [21–25], as shown in Fig. 1(a); here, ε_w and ε_b represent the dielectric constants of potential well materials (corresponding to 3D perovskites) and potential barrier materials (corresponding to the hydrophobic organic cations of 2D perovskites), respectively. Gray ovals represent the polarized charges, which can reduce the Coulomb interaction between the electrons and holes. The barrier materials exhibit a smaller dielectric constant and a larger band gap compared to the well materials [14,26–30]. Both the effective dielectric constant of the whole system (corresponding to 2D perovskites) and the polarized charges are reduced [25,26] due to the penetration of the electric field. Consequently, the Coulomb interaction between the electrons and holes is enhanced and the exciton binding energy is increased, accompanying the emergence of dielectric confinement.

Dielectric confinement not only affects the exciton binding energy, but also adjusts the optical band gap [31,32]. More importantly, it significantly boosts the emission efficiency of 2D perovskite materials [31,32]. Recently, a few reports have emphasized the relationship between dielectric confinement and the properties of quasi-2D perovskites, such as the carrier mobility [33], photoluminescent properties [31], hot carrier cooling [34], electron–phonon coupling [34–36], and Auger recombination [32]. However, as a general guiding principle for the design of quantum well structural materials, research

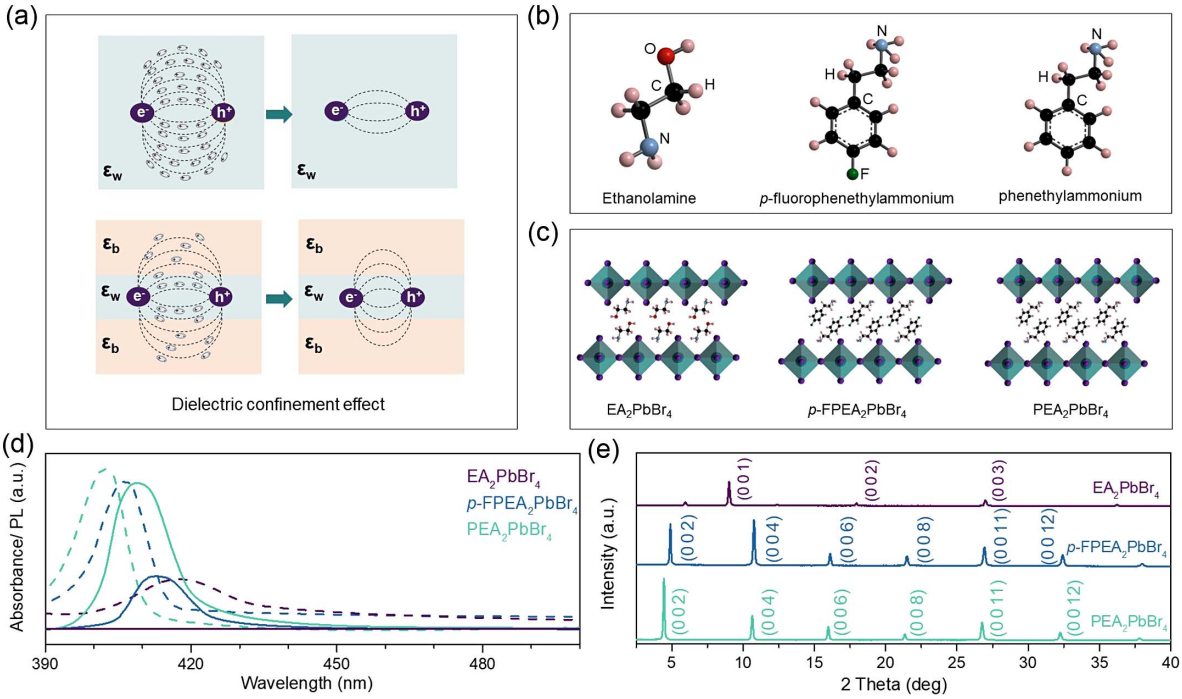

Fig. 1. (a) Schematic illustration of the dielectric confinement effect in a quantum well structure. Note that ε_w is much larger than ε_b. (b) Schematic molecular structures of ethanolamine (EA^+), *p*-fluorophenethylammonium (*p*-$FPEA^+$), and phenethylammonium (PEA^+). (c) Schematic crystal structure of EA_2PbBr_4, *p*-$FPEA_2PbBr_4$, and PEA_2PbBr_4. (d) UV-vis absorption (dashed line) and steady-state PL (solid line) spectra of EA_2PbBr_4, *p*-$FPEA_2PbBr_4$, and PEA_2PbBr_4 perovskite films. (e) XRD patterns of EA_2PbBr_4, *p*-$FPEA_2PbBr_4$, and PEA_2PbBr_4 perovskite films.

on the dielectric confinement effect is still insufficient. For example, it remains unclear how dielectric confinement affects coherent phonon dynamics and how to improve the efficiency. The real-time observation of coherent phonons can provide important insights into electron–phonon coupling [37–39] and exciton dynamics [40]. Besides, the systematic investigation on the influence of dielectric confinement on the physical mechanism in 2D perovskite materials is inadequate.

In this work, we explore the exciton dynamics in quasi-2D Ruddlesden–Popper perovskite (RPP) films containing organic spacers with different dielectric constants, ethanolamine (EA^+), *p*-fluorophenethylammonium (*p*-$FPEA^+$), and phenethylammonium (PEA^+) [31–33], by combining femtosecond pump-probe transient absorption (TA) spectroscopy [41,42] and temperature-dependent PL spectroscopy. The dielectric constant tends to decrease, and the schematic molecular structures are shown in Fig. 1(b). To provide a quantitative comparison, the dielectric constants of EABr, *p*-FPEABr, and PEABr solid powder materials were measured. At 1 GHz, the dielectric constants of EABr, *p*-FPEABr, and PEABr powders are 3.04, 2.90, and 2.74, respectively. The observed trend is consistent with the theoretical predictions [33,43,44]. As expected, the coherent phonon dynamics, the energy transfer process, and the Auger recombination can be tuned by the dielectric confinement effect. Using ligands with small dielectric constants enables the formation of quasi-2D film with a weaker dynamic disorder, resulting in a more complete energy transfer and the inhibition of trap-mediated nonradiative recombination. Furthermore, the increase of the bulk-ligand dielectric constant reduces the corresponding exciton binding energy, thereby suppressing the Auger recombination. Our study will not only improve the radical understanding of exciton dynamics in hybrid layered perovskites but also emphasize the significance of the dielectric confinement effect for exciton dynamics.

2. RESULTS AND DISCUSSION

Quasi-2D RPPs possess the formula of $B_2A_{n-1}Pb_nX_{3n+1}$, where B represents an aromatic or aliphatic alkylammonium cation; A^+ can be an organic or inorganic cation such as methylammonium cation (MA^+) or Cs^+; and X^- is a halide anion. The *n*-values represent the number of inorganic [PbX_6] octahedra sandwiched between organic barriers [13,26,27,32,36]. To precisely explore the influence of the dielectric constant on the coherent phonon dynamics [40] of quasi-2D RPPs, we fabricated $\langle n\rangle = 1$ EA_2PbBr_4, *p*-$FPEA_2PbBr_4$, and PEA_2PbBr_4 perovskite films [Fig. 1(c)] for investigation. (Note: "*n*" stands for the species with a fixed composition and "$\langle n\rangle$" represents the average number of perovskite layers in the film.) Details of the sample preparation are presented in Appendix A. Figure 1(d) shows the normalized UV-vis absorption and steady-state PL spectra of EA_2PbBr_4, *p*-$FPEA_2PbBr_4$, and PEA_2PbBr_4 perovskite films. The results indicate that the photophysical properties of 2D RPP films are influenced by organic cations with different dielectric constants. The three $\langle n\rangle = 1$ films show the characteristic of single exciton absorption peak, indicating a pure phase for these materials. The absorption peak wavelength is blueshifted

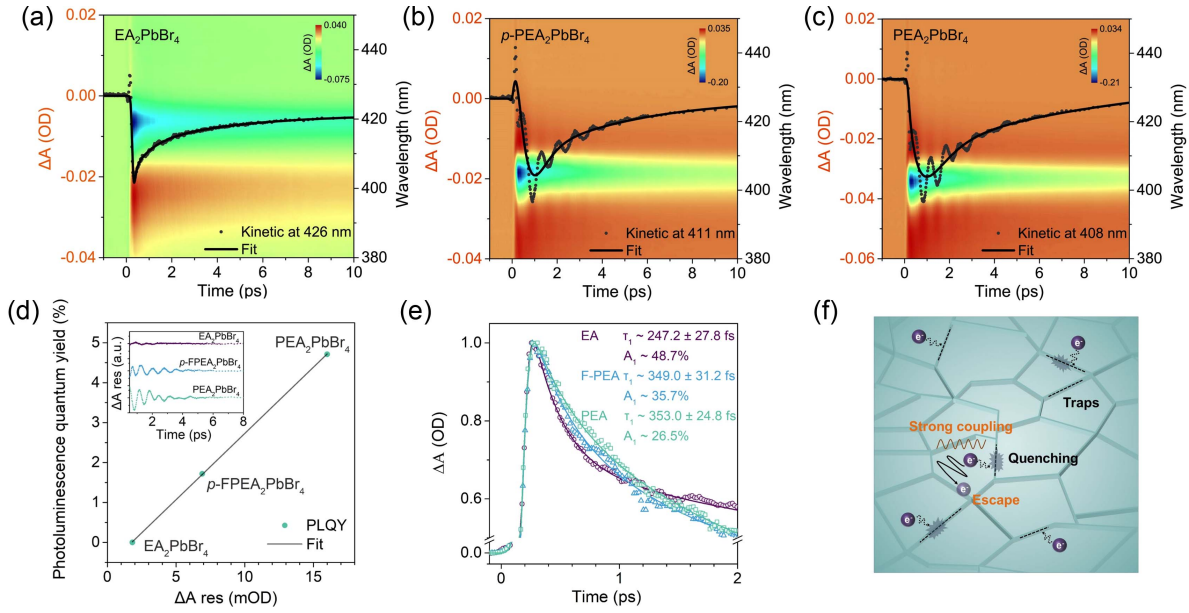

Fig. 2. TA spectra (vis-pseudocolor representation) and TA dynamics (black dots and lines) of a representative probe wavelength for (a) EA_2PbBr_4, (b) p-$FPEA_2PbBr_4$, and (c) PEA_2PbBr_4 perovskite films. Note: The orange coordinate scale corresponds to the TA dynamics of a representative probe wavelength, and the black coordinate scale corresponds to the TA spectra. (d) PLQYs as a function of maximum phonon modulation amplitude. Inset: Coherent phonon dynamics (the residuals after subtracting the contribution of exciton population from origin kinetics) of three perovskite films. (e) Population dynamics of EA_2PbBr_4, p-$FPEA_2PbBr_4$, and PEA_2PbBr_4 perovskite films. (f) Coherent phonon circumvents the defect capture process in perovskite thin films.

in the order of 417.5 nm (EA_2PbBr_4) > 406.0 nm (p-$FPEA_2PbBr_4$) > 402.5 nm (PEA_2PbBr_4). The corresponding PL peak wavelengths reveal a similar trend (412.8 nm for p-$FPEA_2PbBr_4$ > 408.9 nm for PEA_2PbBr_4), except that the emission of EA_2PbBr_4 is too weak to measure. Figure 1(e) depicts the X-ray diffraction (XRD) patterns of EA_2PbBr_4, p-$FPEA_2PbBr_4$, and PEA_2PbBr_4 perovskite films. All of the 2D RPP films are characteristic of a set of (0 0 k) diffraction peaks [31–33], demonstrating the formation of a layered structure.

The broadband pump-probe TA spectroscopy was used to investigate the ultrafast dynamics of 2D RPP EA_2PbBr_4, p-$FPEA_2PbBr_4$, and PEA_2PbBr_4 films. The corresponding TA spectra and dynamics are depicted in Figs. 2(a)–2(c). Note that the orange coordinate scale corresponds to TA dynamics of a representative probe wavelength, and the black coordinate scale corresponds to TA spectra. As shown in Fig. 2(a), the TA spectrum is comprised of one ground state bleaching (GSB, $\Delta A < 0$) peak at 418 nm correlating with the linear absorption spectra and one photoinduced absorption (PIA, $\Delta A > 0$) band at the blue side of the GSB band. Similar phenomena are also observed in p-$FPEA_2PbBr_4$ [Fig. 2(b)] and PEA_2PbBr_4 [Fig. 2(c)] films. Unlike the EA_2PbBr_4 film, obvious coherent oscillations decaying with time due to electron-optical phonon coupling [39,40,45,46] are present in the TA kinetics of p-$FPEA_2PbBr_4$ and PEA_2PbBr_4 films, as shown in black dots of Figs. 2(b) and 2(c). To precisely evaluate the variation trend of coherent phonon dynamics, we fitted TA kinetics with multi-exponential functions [$\Delta A(t) = a_1 \exp(-t/\tau_1) + a_2 \exp(-t/\tau_2) + \ldots + a_n \exp(-t/\tau_n) - c_1 \exp(-t/\tau_{et})$, where $a_1, a_2, \ldots, a_n$, c_1 are amplitudes; $\tau_1, \tau_2, \ldots, \tau_n$ are decay time constants, and τ_{et} is formation time constant], and then obtained the coherent phonon dynamics by subtracting the exciton kinetics, as shown in the inset of Fig. 2(d). The background exciton dynamics is related to rapid electronic excited state relaxation. The τ_1 corresponds to the defect trapping process. The τ_2 is the result of hot carrier cooling and exciton formation processes. The τ_3 is associated with carrier population decay caused by various radiative and nonradiative recombination processes [40,46]. The coherent oscillation time of 2D RPP EA_2PbBr_4 film is short and the modulation depth is weak. Furthermore, the PEA_2PbBr_4 film exhibits superior coherent phonon modulation depth compared to p-$FPEA_2PbBr_4$.

In the process of exploring the relationship between coherent phonon dynamics and luminescence performance, it was observed that the amplitude of phonon dephasing dynamics is positively correlated with photoluminescence quantum yield (PLQY). To further investigate the relationship between coherent phonon dynamics and the luminescence mechanism, a TA kinetic analysis was conducted. As shown in Fig. 2(e), the bleaching kinetics of EA_2PbBr_4, p-$FPEA_2PbBr_4$, and PEA_2PbBr_4 films exhibit a fast decay (τ_1, corresponding to the defect trapping process [47]) under the same experimental conditions. Detailed fitting data for the three films are described in Table 1. As shown in Table 1, the proportion of τ_1 gradually decreases and the lifetime gradually increases as the dielectric constant of the bulk ligand decreases, indicating that trap-assisted recombination is inhibited. Based on these observations, we propose a mechanism for defect screening in the presence of a coherent phonon. Perovskite films contain

Table 1. Fitting Parameters of the GSB Kinetics of $\langle n \rangle = 1$ Quasi-2D RPP Films

	τ_1/fs (Weight/%)	τ_2/ps (Weight/%)	τ_3/ps (Weight/%)
EA_2PbBr_4	247.2 ± 27.8 (48.7)	3.4 ± 0.24 (26.8)	32.9 ± 4.3 (24.5)
p-$FPEA_2PbBr_4$	349.0 ± 31.2 (35.7)	2.7 ± 0.21 (47.5)	26.9 ± 3.5 (16.8)
PEA_2PbBr_4	353.0 ± 24.8 (26.5)	2.3 ± 0.19 (55.6)	21.9 ± 2.3 (17.9)

numerous grain boundaries where most defects are located [35], as shown in Fig. 2(f). When decreasing the dielectric constant of bulk ligand, Coulomb shielding is tuned, and the dynamic disorder is weaker. Excitons are strongly coupled with optical phonons [40], enabling them to screen charge defects and overcome the trap-mediated nonradiative recombination [48,49]. In the case of 3D lead halide perovskites, it has been proposed that electron–phonon coupling (polaron effect) protects photogenerated carriers from lossy scattering paths involving defects and Auger-like processes [45,50–52]. These observations indicate the coherent phonon of quasi-2D perovskites that can also potentially shield the excitons from trap-mediated nonradiative pathways.

Based on the discussion above, $\langle n \rangle = 4$ 2D RPP films, with excellent emission properties according to previous reports [32], were fabricated to further investigate exciton dynamics. Figure 3(a) shows the PL and absorption spectra of the $\langle n \rangle = 4$ thin films using the three dielectric constant bulk ligands. Unlike the $\langle n \rangle = 1$ 2D RPP films, multiple absorption peaks appear in the steady-state absorption spectra of $\langle n \rangle = 4$ films, indicating the distribution of a series of quantum wells instead of a pure phase [44]. The large-*n* quantum well absorption peak of the $EA_2MA_3Pb_4Br_{13}$ film is blueshifted compared to *p*-$FPEA_2MA_3Pb_4Br_{13}$ and $PEA_2MA_3Pb_4Br_{13}$ perovskite films, which is attributed to the difference in the domain distribution [29,32,44]. The characteristics of steady-state PL

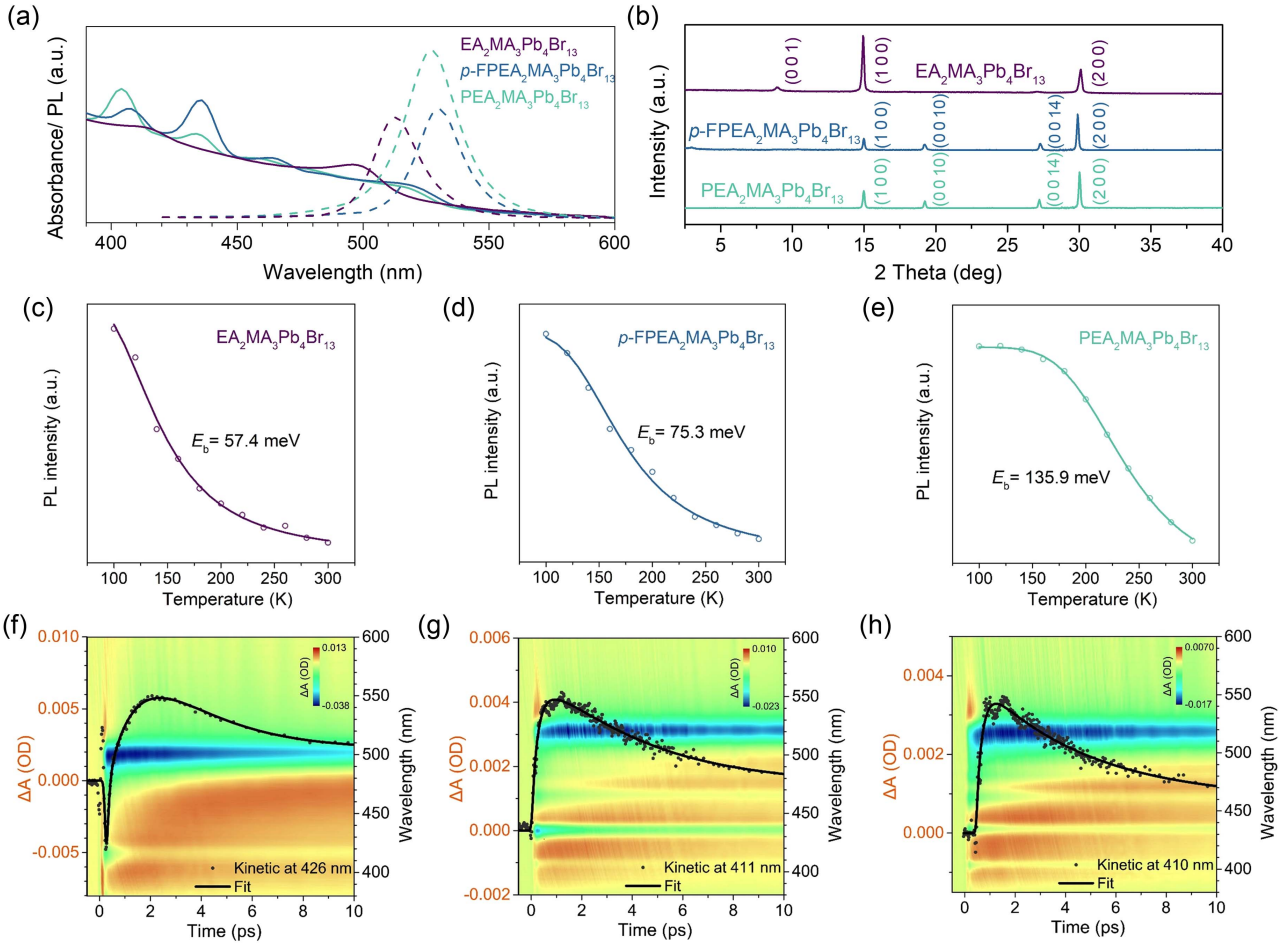

Fig. 3. (a) UV-vis absorption (dashed line) and steady-state PL (solid line) spectra of $EA_2MA_3Pb_4Br_{13}$, *p*-$FPEA_2MA_3Pb_4Br_{13}$, and $PEA_2MA_3Pb_4Br_{13}$ perovskite films. (b) XRD patterns of $EA_2MA_3Pb4Br_{13}$, *p*-$FPEA_2MA_3Pb_4Br_{13}$, and $PEA_2MA_3Pb_4Br_{13}$ perovskite films. Temperature-dependent integrating PL intensity at different temperatures and corresponding fitting curves for (c) $EA_2MA_3Pb_4Br_{13}$, (d) *p*-$FPEA_2MA_3Pb_4Br_{13}$, and (e) $PEA_2MA_3Pb_4Br_{13}$ perovskite films. TA spectra (vis-pseudocolor representation) and TA dynamics (black dots and lines) of a representative probe wavelength for (f) $EA_2MA_3Pb_4Br_{13}$, (g) *p*-$FPEA_2MA_3Pb_4Br_{13}$, and (h) $PEA_2MA_3Pb_4Br_{13}$ perovskite films. Note: The orange ordinate scale corresponds to TA dynamics of a representative probe wavelength, and the black ordinate scale corresponds to TA spectra.

spectra are consistent with those of steady-state absorption spectra. The XRD patterns of $EA_2MA_3Pb_4Br_{13}$, *p*-$FPEA_2MA_3Pb_4Br_{13}$, and $PEA_2MA_3Pb_4Br_{13}$ are presented in Fig. 3(b). The (0 0 *k*) diffraction peaks derived from $n = 1$ species can be observed in $\langle n\rangle = 4$ perovskites, demonstrating the formation of a layered structure. In addition, the diffraction peaks of high *n* space appear, which confirms the mixed phase within the quasi-2D perovskite films [32]. Furthermore, temperature-dependent PL measurements were performed to quantitatively extract the E_b [Figs. 3(c)–3(e)] [32,53]. With the increase in temperature, the PL spectra exhibit features of intensity reduction and spectral line broadening. The exciton binding energy of the perovskite film is evaluated by the temperature dependence of the PL-signal integral intensity [43], and is fitted using [16,32,43]

$$I(T) = \frac{I_0}{1 + Ae^{\frac{-E_b}{k_B T}}}, \tag{1}$$

where I_0 is the integrated PL intensity extrapolated at 0 K, A is a constant, E_b is the exciton binding energy, and k_B is the Boltzmann constant. The extracted E_b is estimated to be 57.4, 75.3, and 135.9 meV for $EA_2MA_3Pb_4Br_{13}$, *p*-$FPEA_2MA_3Pb_4Br_{13}$, and $PEA_2MA_3Pb_4Br_{13}$, respectively. The results confirm that decreasing the dielectric constant of the ligand will increase E_b [32,33]. Basically, organic ligands possessing small dielectric constants exhibit reduced polarity, which diminishes the dielectric screening of electron–hole interactions and consequently leads to dielectric confinement. Thus, it becomes feasible to reduce E_b by attenuating the dielectric confinement.

To investigate the ultrafast exciton dynamics in quasi-2D RPP $EA_2MA_3Pb4Br_{13}$, *p*-$FPEA_2MA_3Pb_4Br_{13}$, and $PEA_2MA_3Pb_4Br_{13}$ films, TA measurements, as shown in Figs. 3(f)–3(h), were conducted. The orange coordinate scale corresponds to the TA dynamics of a representative probe wavelength, and the black coordinate scale corresponds to the TA spectra. With the exception of $EA_2MA_3Pb_4Br_{13}$ films, the coherent phonon dynamics similar to $\langle n\rangle = 1$ films were observed in $\langle n\rangle = 4$ quasi-2D perovskite films, and the strongest TA oscillatory kinetics of the three spectra were extracted, respectively. The variation trend of phonon dephasing dynamics is consistent with that of $\langle n\rangle = 1$ films, in which the material with the lowest dielectric constant has the largest modulation depth of a coherent phonon.

TA spectra at representative delay times of $EA_2MA_3Pb_4Br_{13}$, *p*-$FPEA_2MA_3Pb_4Br_{13}$, and $PEA_2MA_3Pb_4Br_{13}$ perovskite films were extracted to investigate the influence of coherent phonon dynamics on energy transfer. Figures 4(a)–4(c) depict the TA spectra corresponding to the beginning and end of energy transfer process in the three $\langle n\rangle = 4$ quasi-2D RPP films, respectively. The beginning and end times of the energy transfer were selected based on the instrument response function (IRF, ~120 fs) and the maximum point of exciton population, respectively. We then calculated the transfer rate according to the decrease of the small-*n* QWs ($n \le 5$) population and the increase of large-*n* QWs ($n > 5$) to evaluate energy loss quantitatively. To reduce errors, the signal fluctuation caused by the excited state absorption is removed, and the detailed data are described in Table 2. As shown, the transfer rate increases from 35.5%,

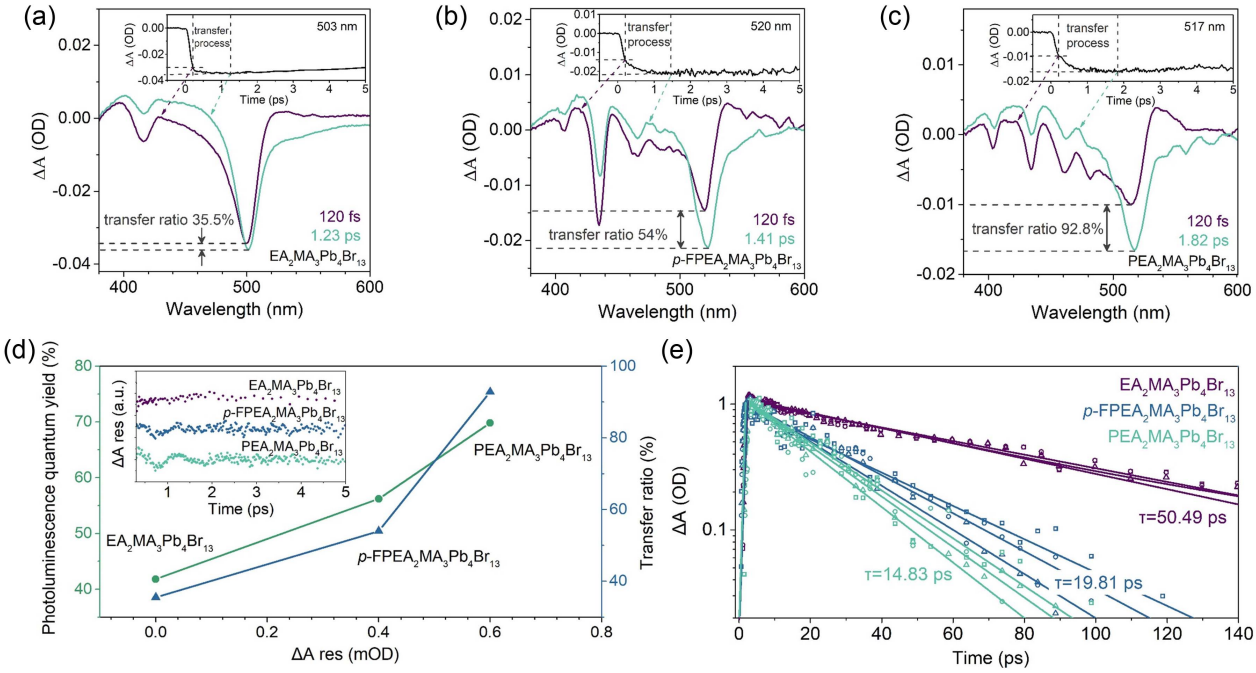

Fig. 4. (a)–(c) TA spectra at representative delay times of $EA_2MA_3Pb_4Br_{13}$, *p*-$FPEA_2MA_3Pb_4Br_{13}$, and $PEA_2MA_3Pb_4Br_{13}$ perovskite films, respectively. Inset: Transfer processes in population dynamics of three perovskite films. (d) PLQYs as a function of maximum phonon modulation amplitude. Inset: Coherent phonon dynamics of the three perovskite films. (e) Biexciton Auger recombination kinetics. The circles, squares, and triangles represent the two-by-two subtraction (P_2–P_1, P_3–P_2, and P_3–P_1) from the TA population dynamics at three different pump fluences (P_1, P_2, and P_3). The biexciton Auger recombination lifetime (τ) is obtained by averaging the three time constants from the fittings using a single exponential function.

Table 2. Variation (ΔA, the last value − the initial value) of TA Population Dynamics and Transfer Ratio for $EA_2MA_3Pb_4Br_{13}$, *p*-$FPEA_2MA_3Pb_4Br_{13}$, and $PEA_2MA_3Pb_4Br_{13}$ Perovskite Films

	$\Delta A_{n=1}$ (mOD)	$\Delta A_{n=2}$ (mOD)	$\Delta A_{n=3}$ (mOD)	$\Delta A_{n=4}$ (mOD)	$\Delta A_{n=\infty}$ (mOD)	Transfer Ratio (%)
$EA_2MA_3Pb_4Br_{13}$	−4.7	—	—	—	—	35.5
p-$FPEA_2MA_3Pb_4Br_{13}$	−1.3	−7.4	−3.2	−0.5	6.7	54.0
$PEA_2MA_3Pb_4Br_{13}$	−1.4	−2.8	−2.4	−0.4	6.5	92.8

54%, and 92.8% after the modulation depth of the coherent phonon increases (the bulk ligand dielectric constant decreases), further indicating that coherent phonons have the potential to screen charge defects and improve energy transfer efficiency. Figure 4(d) presents the evolution of PLQY and energy transfer rate as a function of the modulation depth. The results show that the modulation depth of a coherent phonon is positively correlated with PLQY and the energy transfer rate. It can be inferred that an effective competition exists between coherent phonon dynamics and trap-mediated nonradiative recombination in quasi-2D RPP films.

Auger recombination, as an important factor in exciton dynamics, has a crucial impact on the performance of infrared detectors, the efficiency roll-off of light-emitting diodes, and the transport properties of topological insulators [54,55]. The recombination dynamics of GSB under different pump fluences were investigated to explore the Auger recombination kinetics. Notably, a fast decay component grows rapidly as the pump fluence increases, which is consistent with the characteristic of biexciton recombination [56–58]. The biexciton Auger recombination lifetime (τ) was obtained by performing a two-by-two subtraction (P_2–P_1, P_3–P_2, and P_3–P_1) from the TA population dynamics at three different pump fluences (P_1, P_2, and P_3) and then averaging the three fitted time constants. As shown in Fig. 4(e), the time constants of $EA_2MA_3Pb_4Br_{13}$, *p*-$FPEA_2MA_3Pb_4Br_{13}$, and $PEA_2MA_3Pb_4Br_{13}$ perovskite films are 50.49, 19.81, and 14.83 ps, respectively. This analysis confirms that the increase in the bulk-ligand dielectric constant reduces the corresponding exciton binding energy, thereby suppressing the Auger recombination [54,56,59]. These results demonstrate the potential use of the dielectric constant as a regulator of exciton dynamics in perovskite materials.

3. CONCLUSION

In summary, we selected three large cations with different dielectric constants as the ligands of quasi-2D RPPs and studied the corresponding coherent phonon dynamics, energy transfer process, and Auger recombination dynamics of $\langle n \rangle = 1$ and 4 thin films. By correlating the dielectric confinement effect with exciton dynamics, we found that the use of ligands with a smaller dielectric constant can reduce the screening of Coulomb interaction and weaken dynamic disorder, resulting in coherent phonons with a higher modulation depth. The TA kinetics under different dielectric constant ligands and with different $\langle n \rangle$ indicate that the coherent phonons can effectively screen the trap-mediated nonradiative relaxation path, increase the energy transfer rate, and obtain a higher PLQY. Note that the transfer rate increases to 35.5%, 54%, and 92.8% after the modulation depth of the coherent phonons increases. Furthermore, the TA GSB kinetics under different pump fluences of $\langle n \rangle = 4$ films with various dielectric constants confirm that Auger recombination can be suppressed by increasing the bulk ligand dielectric constant. The time constants of biexciton recombination kinetics are 50.49, 19.81, and 14.83 ps for $EA_2MA_3Pb_4Br_{13}$, *p*-$FPEA_2MA_3Pb_4Br_{13}$, and $PEA_2MA_3Pb_4Br_{13}$ perovskite films, respectively. By increasing the dielectric constant, the contribution of the Auger recombination can be reduced for realizing stable devices under high current density. This work emphasizes the importance of the dielectric constant in quasi-2D perovskite material design and may provide valuable insights into the exciton dynamics of organic–inorganic hybrid layered perovskite relevant for emergent optoelectronics development.

APPENDIX A: MATERIALS AND METHODS

$PbBr_2$ was purchased from Sigma-Aldrich, and PEABr, *p*-FPEABr, EABr, and MABr were obtained from Greatcell Solar. Dimethyl sulfoxide (DMSO, chromatographic grade) was purchased from Aladdin. The materials were used directly without any further purification.

Different quasi-2D RPP $EA_2MA_{n-1}Pb_nBr_{3n+1}$ (*p*-$FPEA_2MA_{n-1}Pb_nBr_{3n+1}$ or $PEA_2MA_{n-1}Pb_nBr_{3n+1}$) precursor solutions were prepared by dissolving stoichiometric quantities of EABr (*p*-FPEABr or PEABr), MABr, and $PbBr_2$ in DMSO as the solvent, stirring under ambient conditions for 2 h. Subsequently, the various precursor solutions were coated onto a quartz substrate via a one-step spin-coating process at 4000 r/min for 50 s, respectively. The as-prepared films were annealed at 80°C for 10 min. All the materials were prepared in a glove box under a nitrogen atmosphere.

The dielectric constants (real part of the complex permittivity) of EABr, *p*-FPEABr, and PEABr solid powder materials were measured using a vector network analyzer (Agilent E5071C). The XRD patterns of perovskite films were recorded using a Bruker D8 diffractometer with Cu Kα radiation. The steady-state absorption spectra were characterized by a dual-beam spectrophotometer (Cary-5000, Agilent). For the steady-state PL measurements, a 400 nm pump laser was produced by focusing a portion of the fundamental 800 nm laser pulses (Coherent, 800 nm, 1 kHz, 7 mJ $pulse^{-1}$, 35 fs) onto a BBO crystal. The 400 nm pump laser was directed vertically onto the thin films, and the emission from the film edges was vertically collected and detected with a fiber spectrometer (USB-4000, Ocean Optics). Temperature-dependent PL measurements were conducted using a liquid nitrogen thermostat (Lanhai Instrument, LNC-W). A 405 nm laser with a power of 2 μW was employed to excite the samples. The PLQY was measured by a Quanta-Phi integrating sphere, which was an optical fiber

bundle coupled with a Fluorolog system. The corresponding excitation wavelength was set as 365 nm, and the excitation intensity was 1.5 mW cm^{-2}.

The femtosecond-TA measurements were collected using a Helios pump-probe system (Ultrafast Systems). Pump pulses of different wavelengths were generated from an optical parametric amplifier (TOPAS-800-fs). White-light continuum probe pulses (380–600 nm) were produced by focusing a portion of the fundamental 800 nm laser pulses (Coherent, 800 nm, 1 kHz, 7 mJ $pulse^{-1}$, 35 fs) onto a calcium fluoride crystal. The samples were measured with probing polarizations oriented at the magic angle. Furthermore, pump-fluence-dependent TA measurements were performed using a neutral density filter to change the pump intensity. The instrument response function was determined to be ∼120 fs through a routine cross-correlation procedure.

Funding. National Natural Science Foundation of China (12347158, 11804084, 12074104, 61627818, U1804261); Natural Science Foundation of Henan Province (222300420057); Young Backbone Teacher Training Program in Higher Education of Henan Province (2019GGJS065).

Disclosures. The authors declare no conflicts of interest.

Data Availability. Data underlying the results presented in this paper are not publicly available at this time but may be obtained from the authors upon reasonable request.

REFERENCES

1. N. Li, X. Niu, L. Li, *et al.*, "Liquid medium annealing for fabricating durable perovskite solar cells with improved reproducibility," Science **373**, 561–567 (2021).
2. L. Wang, H. Zhou, J. Hu, *et al.*, "A Eu^{3+}-Eu^{2+} ion redox shuttle imparts operational durability to Pb-I perovskite solar cells," Science **363**, 265–270 (2019).
3. Z. Liu, W. Qiu, X. Peng, *et al.*, "Perovskite light-emitting diodes with EQE exceeding 28% through a synergetic dual-additive strategy for defect passivation and nanostructure regulation," Adv. Mater. **33**, 2103268 (2021).
4. X. Liu, W. Xu, S. Bai, *et al.*, "Metal halide perovskites for light-emitting diodes," Nat. Mater. **20**, 10–21 (2021).
5. K. Lin, J. Xing, N. Q. Li, *et al.*, "Perovskite light-emitting diodes with external quantum efficiency exceeding 20 percent," Nature **562**, 245–248 (2018).
6. C. Yu, N. Wang, T. He, *et al.*, "Perovskite light-emitting diodes based on spontaneously formed submicrometre-scale structures," Nature **562**, 249–253 (2018).
7. Y. Hassan, J. H. Park, M. L. Crawford, *et al.*, "Ligand-engineered bandgap stability in mixed-halide perovskite LEDs," Nature **591**, 72–77 (2021).
8. Y. Liu, J. Cui, K. Du, *et al.*, "Efficient blue light-emitting diodes based on quantum-confined bromide perovskite nanostructures," Nat. Photonics **13**, 760–764 (2019).
9. G. Xing, N. Mathews, S. S. Lim, *et al.*, "Low-temperature solution-processed wavelength-tunable perovskites for lasing," Nat. Mater. **13**, 476–480 (2014).
10. Q. Zhang, Q. Shang, R. Su, *et al.*, "Halide perovskite semiconductor lasers: materials, cavity design, and low threshold," Nano Lett. **21**, 1903–1914 (2021).
11. S. C. Hou, M. K. Gangishetty, Q. M. Quan, *et al.*, "Efficient blue and white perovskite light-emitting diodes via manganese doping," Joule **2**, 2421–2433 (2018).
12. M. K. Gangishetty, S. C. Hou, Q. M. Quan, *et al.*, "Reducing architecture limitations for efficient blue perovskite light-emitting diodes," Adv. Mater. **30**, 1706226 (2018).
13. M. Cui, C. Qin, Y. Jiang, *et al.*, "Direct observation of competition between amplified spontaneous emission and Auger recombination in quasi-two-dimensional perovskites," J. Phys. Chem. Lett. **11**, 5734–5745 (2020).
14. T. He, S. Li, Y. Jiang, *et al.*, "Reduced-dimensional perovskite photovoltaics with homogeneous energy landscape," Nat. Commun. **11**, 1672 (2020).
15. C. T. Zuo, A. Scully, D. Yak, *et al.*, "Self-assembled 2D perovskite layers for efficient printable solar cells," Adv. Energy Mater. **9**, 1803258 (2019).
16. M. J. Yuan, L. N. Quan, R. Comin, *et al.*, "Perovskite energy funnels for efficient light-emitting diodes," Nat. Nanotechnol. **11**, 872–877 (2016).
17. X. Gong, O. Voznyy, A. Jain, *et al.*, "Electron-phonon interaction in efficient perovskite blue emitters," Nat. Mater. **17**, 550–556 (2018).
18. H. H. Tsai, W. Y. Nie, J. C. Blancon, *et al.*, "High-efficiency two-dimensional Ruddlesden–Popper perovskite solar cells," Nature **536**, 312–316 (2016).
19. Y. Zhang, J. Wen, Z. Xu, *et al.*, "Effective phase-alignment for 2D halide perovskites incorporating symmetric diammonium ion for photovoltaics," Adv. Sci. **8**, 2001433 (2021).
20. D. Ma, K. Lin, Y. Dong, *et al.*, "Distribution control enables efficient reduced-dimensional perovskite LEDs," Nature **599**, 594–598 (2021).
21. X. Yang, X. Zhang, J. Deng, *et al.*, "Efficient green light-emitting diodes based on quasi-two-dimensional composition and phase engineered perovskite with surface passivation," Nat. Commun. **9**, 570 (2018).
22. R. L. Milot, R. J. Sutton, G. E. Eperon, *et al.*, "Charge carrier dynamics in 2D hybrid metal halide perovskites," Nano Lett. **16**, 7001–7007 (2016).
23. N. Wang, C. Lu, G. Rui, *et al.*, "Perovskite light-emitting diodes based on solution-processed self-organized multiple quantum wells," Nat. Photonics **10**, 699–704 (2016).
24. C. Qin, T. Matsushima, and W. Potscavage, Jr., "Triplet management for efficient perovskite light-emitting diodes," Nat. Photonics **14**, 70–75 (2020).
25. M. Kumagai and T. Takagahara, "Excitonic and nonlinear-optical properties of dielectric quantum-well structures," Phys. Rev. B **40**, 12359–12381 (1989).
26. G. Wu, R. Liang, Z. Zhang, *et al.*, "2D hybrid halide perovskites: structure, properties, and applications in solar cells," Small **17**, 2103514 (2021).
27. Y. Jiang, C. Qin, M. Cui, *et al.*, "Spectra stable blue perovskite light-emitting diodes," Nat. Commun. **10**, 1868 (2019).
28. C. Sun, Y. Jiang, M. Cui, *et al.*, "High-performance large-area quasi-2D perovskite light-emitting diodes," Nat. Commun. **12**, 2207 (2021).
29. Y. Tian, X. Qian, C. Qin, *et al.*, "Modulating low-dimensional domains of self-assembling quasi-2D perovskites for efficient and spectra-stable blue light-emitting diodes," Chem. Eng. J **415**, 129088 (2021).
30. Y. Jin, Z. Wang, S. Yuan, *et al.*, "Synergistic effect of dual ligands on stable blue quasi-2D perovskite light-emitting diodes," Adv. Funct. Mater. **30**, 1908339 (2020).
31. J. T. Lin, C. C. Liao, C. S. Hsu, *et al.*, "Harnessing dielectric confinement on tin perovskites to achieve emission quantum yield up to 21%," J. Am. Chem. Soc. **141**, 10324–10330 (2019).
32. Y. Jiang, M. Cui, S. Li, *et al.*, "Reducing the impact of Auger recombination in quasi-2D perovskite light-emitting diodes," Nat. Commun. **12**, 336 (2021).
33. B. Cheng, T. Y. Li, P. Maity, *et al.*, "Extremely reduced dielectric confinement in two-dimensional hybrid perovskites with large polar organics," Commun. Phys. **1**, 80 (2018).
34. J. Yin, P. Maity, R. Naphade, *et al.*, "Tuning hot carrier cooling dynamics by dielectric confinement in two-dimensional hybrid perovskite crystals," ACS Nano **13**, 12621–12629 (2019).
35. R. Su, Z. Xu, J. Wu, *et al.*, "Dielectric screening in perovskite photovoltaics," Nat. Commun. **12**, 2479 (2021).
36. C. Song, H. Yang, F. Liu, *et al.*, "Ultrafast femtosecond pressure modulation of structure and exciton kinetics in 2D halide perovskites for enhanced light response and stability," Nat. Commun. **12**, 4879 (2021).

37. Q. Du, C. Zhu, Z. Yin, *et al.*, "Stacking effects on electron–phonon coupling in layered hybrid perovskites via microstrain manipulation," ACS Nano **14**, 5806–5817 (2020).
38. W. Tao, C. Zhang, Q. Zhou, *et al.*, "Momentarily trapped exciton polaron in two-dimensional lead halide perovskites," Nat. Commun. **12**, 1400 (2021).
39. M. Cui, C. Qin, Z. Zhou, *et al.*, "Tuning coherent phonon dynamics in two-dimensional phenylethylammonium lead bromide perovskites," Nano Res. **16**, 3408–3414 (2023).
40. L. N. Quan, Y. Park, P. Guo, *et al.*, "Vibrational relaxation dynamics in layered perovskite quantum wells," Proc. Natl. Acad. Sci. USA **118**, e2104425118 (2021).
41. C. Qin, M. Cui, D. Song, *et al.*, "Ultrafast multiexciton Auger recombination of CdSeS," Acta Phys. Sin. **68**, 107801 (2019).
42. K. Zhang, M. Niu, Z. Jiang, *et al.*, "Multiple temporal-scale photocarrier dynamics induced by synergistic effects of fluorination and chlorination in highly efficient nonfullerene organic solar cells," Sol. RRL **4**, 1900552 (2020).
43. X. Hong, T. Ishihara, and A. V. Nurmikko, "Dielectric confinement effect on excitons in PbI_4-based layered semiconductors," Phys. Rev. B **45**, 6961–6964 (1992).
44. J. Hu, I. W. H. Oswald, S. J. Stuard, *et al.*, "Synthetic control over orientational degeneracy of spacer cations enhances solar cell efficiency in two-dimensional perovskites," Nat. Commun. **10**, 1276 (2019).
45. F. Thouin, D. A. Valverde-Chavez, C. Quarti, *et al.*, "Phonon coherences reveal the polaronic character of excitons in two-dimensional lead halide perovskites," Nat. Mater. **18**, 349–354 (2019).
46. J. Fu, M. Li, A. Solanki, *et al.*, "Electronic states modulation by coherent optical phonons in 2D halide perovskites," Adv. Mater. **33**, 2006233 (2021).
47. L. N. Quan, Y. Zhao, G. D. Pelayo, *et al.*, "Tailoring the energy landscape in quasi-2D halide perovskites enables efficient green-light emission," Nano Lett. **17**, 3701–3709 (2017).
48. R. Long, L. Jin, and O. V. Prezhdo, "Unravelling the effects of grain boundary and chemical doping on electron-hole recombination in $CH_3NH_3PbI_3$ perovskite by time-domain atomistic simulation," J. Am. Chem. Soc. **138**, 3884–3890 (2016).
49. S. Martin, P. Samuel, and G. Feliciano, "Carrier lifetimes and polaronic mass enhancement in the hybrid halide perovskite $CH_3NH_3PbI_3$ from multiphonon Fröhlich coupling," Phys. Rev. Lett. **121**, 086402 (2018).
50. D. Zhao, H. Hu, R. Haselsberger, *et al.*, "Monitoring electron-phonon interactions in lead halide perovskites using time-resolved THz spectroscopy," ACS Nano **13**, 8826–8835 (2019).
51. H. Zhu, K. Miyata, Y. Fu, *et al.*, "Screening in crystalline liquids protects energetic carriers in hybrid perovskites," Science **353**, 1409–1413 (2016).
52. K. Miyata, D. Meggiolaro, M. T. Tuan, *et al.*, "Large polarons in lead halide perovskites," Sci. Adv. **3**, e1701217 (2017).
53. Z. Guo, Y. Zhang, B. Wang, *et al.*, "Promoting energy transfer via manipulation of crystallization kinetics of quasi-2D perovskites for efficient green light-emitting diodes," Adv. Mater. **33**, 2102246 (2021).
54. C. Wang, G. Dai, J. Wang, *et al.*, "Low-threshold blue quasi-2D perovskite laser through domain distribution control," Nano Lett. **22**, 1338–1344 (2022).
55. X. Zhang, J. X. Shen, and C. G. Van de Walle, "Anomalous Auger recombination in PbSe," Phys. Rev. Lett. **125**, 037401 (2020).
56. V. I. Klimov, A. A. Mikhailovsky, D. W. McBranch, *et al.*, "Quantization of multiparticle Auger rates in semiconductor quantum dots," Science **287**, 1011–1013 (2000).
57. Y. Li, T. Ding, X. Luo, *et al.*, "Biexciton Auger recombination in monodispersed, quantum-confined $CsPbBr_3$ perovskite nanocrystals obeys universal volume-scaling," Nano Res. **12**, 619–623 (2019).
58. Y. Li, X. Luo, T. Ding, *et al.*, "Size and halide dependent Auger recombination in lead halide perovskite nanocrystals," Angew. Chem. Int. Ed. **59**, 14292–14295 (2020).
59. A. Hangleiter and R. Häcker, "Enhancement of band-to-band Auger recombination by electron-hole correlations," Phys. Rev. Lett. **65**, 215–218 (1990).